ORIGINAL ARTICLE

Identification of a CEACAM5 targeted nanobody for positron emission tomography imaging and near-infrared fluorescence imaging of colorectal cancer

Yitai Xiao[1,2] · Chaoming Mei[1,2] · Duo Xu[1,2] · Fan Yang[1,2] · Meilin Yang[1,2] · Lei Bi[2] · Junjie Mao[3] · Pengfei Pang[3] · Dan Li[1,2]

Abstract

Purpose Here, we aim to identify a CEACAM5-targeted nanobody and demonstrate its application in positron emission tomography (PET) imaging and near-infrared (NIR) fluorescence imaging in colorectal cancer (CRC).

Methods Immunohistochemistry was applied to verify CEACAM5 expression in CRC and metastatic lymph nodes (mLNs). CEACAM5-targeted nanobodies were obtained by immunization of human CEACAM5 protein in a dromedary, followed by several rounds of phage screenings. Immunofluorescence staining and flow cytometry was carried out to determine the binding affinity of the nanobodies. The nanobodies were radiolabeled by coupling ^{18}F-SFB for PET imaging of CRC subcutaneous xenografts and lymph node metastasis (LNM). IRDye800CW (IR800) were conjugated to form NIR probes for NIR imaging in CRC subcutaneous models.

Results CEACAM5 was overexpressed in either human CRC tissues or mLNs. A CEACAM5 targeted nanobody, Nb41 was successfully generated, with excellent *in vitro* binding properties. Incorporation of albumin binding domain (ABD) did not affect the affinity of Nb41. *In vivo* imaging showed that both ^{18}F-FB-Nb41 and ^{18}F-FB-Nb41-ABD showed obvious accumulation in the tumor. Due to the longer retention in the blood, ^{18}F-FB-Nb41-ABD enrichment in tumors was significantly delayed but higher compared to ^{18}F-FB-Nb41. Both ^{18}F-FB-Nb41 and ^{18}F-FB-Nb41-ABD showed prominent LNM enrichment. Similarly, the IR800-conjugated nanobodies Nb41-IR800 and Nb41-ABD-IR800 exhibited superior imaging effects in subcutaneous models, while Nb41-ABD-IR800 exhibited higher fluorescence intensity in the tumor accompanied with a remarkedly delay compared to Nb41-IR800.

Conclusion Collectively, we presented the identification and *in vivo* validation of a CEACAM5-targeted nanobody and a fused nanobody with an ABD, which enabled to the non-invasive visualization of malignancy of CRC using PET imaging and NIR imaging in subcutaneous models as well as LNM models.

Keywords CEACAM5 · Nanobody · Positron emission tomography imaging · Near-infrared fluorescence imaging · Colorectal cancer

---

This article is part of the Topical Collection on Preclinical Imaging.

Yitai Xiao, Chaoming Mei and Duo Xu These authors contributed equally.

✉ Junjie Mao
  maojunj@mail.sysu.edu.cn

✉ Pengfei Pang
  pangpf@mail.sysu.edu.cn

✉ Dan Li
  lidan25@mail.sysu.edu.cn

[1] Department of Nuclear Medicine, The Fifth Affiliated Hospital, Sun Yat-Sen University, Guangdong Province 519000, China

[2] Guangdong Provincial Key Laboratory of Biomedical Imaging and Guangdong Provincial Engineering Research Center of Molecular Imaging, The Fifth Affiliated Hospital, Sun Yat-Sen University, Guangdong Province 519000, China

[3] Center for Interventional Medicine, The Fifth Affiliated Hospital, Sun Yat-Sen University, Guangdong Province 519000, China

Introduction

Colorectal cancer (CRC), one of the most common malignancies ranked third in cancer incidence and second in cancer mortality, accounted for approximately 10% of worldwide diagnosed cancers each year [1]. Surgical excision is considered to be the standard therapeutic modality for patients with localized lesions. Accurate preoperative assessment of tumor borders and local lymph node metastasis (LNM) is essential for precise surgical resection and maximum maintenance of normal physiological function. Nevertheless, 35% of patients already developed LNM or distant metastasis at the time of initial diagnosis, with surgical intervention may be potentially counterproductive [2]. Accurate initial staging and identification of metastatic lesions of CRC using a rapid and non-invasive approach would be indispensable for mapping out tailored treatment regimens.

As a clinically validated method for tumor detection, positron emission tomography (PET) has a transformational impact on presurgical staging and longitudinal monitoring of CRC patients. ^{18}F-fluorodeoxyglucose (FDG) has been widely applied in the evaluation of malignancies based on the ability of detecting increased glycolysis in tumor lesions [3]. However, increased ^{18}F-FDG uptake is also presented in benign lesions, inflammation or granulomas, as well as in normal physiological sites of tracer biodistribution, which may be incorrectly attributed to the etiology of cancer [4]. Molecular probe-based PET imaging is expected to overcome this challenge. Near-infrared fluorescence (NIR) imaging, owing to its potential to delineate tumor margins in real-time and enhance contrast for identification of the lesion during surgery, has been demonstrated to be a promising approach for image-guided resection of tumor and LNM [5]. The complementary nature of the two imaging modalities contributes to a better CRC management, that is, PET imaging allows non-invasive characterization of the disease extent to determine whether a patient is suitable for surgery, while intraoperative NIR imaging helps surgeons demarcate tumor margins thus facilitating more complete tumor resection.

Carcinoembryonic antigen cell adhesion molecule 5 (CEACAM5), also known as CEA, is a highly glycosylated macromolecule belonging to the carcinoembryonic antigen (CEA) family [6]. First recognized as a colorectal tumor-associated antigen decades ago, CEACAM5 has long been considered as an appealing CRC target since it is highly expressed almost exclusively in CRC at high antigenic density and shows limited expression in normal tissues [7]. Thus, the ability of non-invasive imaging of CEACAM5 expression would facilitate precise depiction and accurate diagnosis of CRC.

So far, monoclonal antibodies (mAbs) have been considered to be the best paradigm for the development of high-affinity molecular probes. Nevertheless, the larger molecular weight seems to be the Achilles' heel of mAbs since it often fails to penetrate solid tumor [8]. Intact antibodies often take several days to reach peak enrichment in tumors [9, 10], which are not suitable for use as imaging agents. The advent of phage display has made it possible to customize an antigen-binding domain that is much smaller than an intact mAb [11, 12]. Nanobody, the smallest intact antigen-binding fragment naturally derived from Camelidae family, provides an attractive alternative attributed to the small molecular weight [13]. The smaller size imparts increased permeability, which also leads, however, to their rapid blood clearance and often limited deposition in the tumor. An optional approach is to attach an albumin-binding domain (ABD) to the nanobody, which retains antigen-binding ability while serum clearance is greatly reduced by its constant binding to albumin *in vivo* [14]. This unique feature has enabled applications of nanobodies in facilitating studies of PET imaging and NIR imaging.

In this study, as the preliminary step towards the clinic, we aim to identify a CEACAM5-targeted nanobody and present its application in PET imaging and NIR imaging of CRC. A CEACAM5 targeted nanobody and its ABD fused nanobody, were successfully generated, with excellent *in vitro* binding properties. The immunoconjugates enabled for the non-invasive visualization of malignancy of CRC using PET and NIR imaging in subcutaneous models. These new targeted probes may be of great value for staging guidance and surgical intervention in CRC patients.

Materials and methods

Generation, expression and purification of nanobodies

Nanobodies against CEACAM5 were generated according to previous methods [15]. Briefly, the anti-CEACAM5 nanobodies were selected by several rounds of phage selection, biopannings and enzyme-linked immunosorbent assay (ELISA) screenings. The selected plasmids were transformed into BL21(DE3) competent cells. Cells were cultured at 37 °C till an $OD_{600\,nm}$ reached 0.6 and then induced by adding IPTG at 16 °C. The periplasmic extract obtained after repeated ultrasonic decomposition was centrifugated and loaded on a Ni–NTA Superflow Sepharose column (GE, USA) and further purified by size-exclusion chromatography (SEC). The purity of the proteins was evaluated by sodium dodecyl sulfate polyacrylamide gel electrophoresis (SDS-PAGE) and Coomassie blue staining.

Enzyme-linked immunosorbent assay

A total of 200 ng of human recombinant CEACAM5 protein were coated in a 96-well plate overnight at 4 °C and uncoated protein was washed. After blocking, different concentrations of nanobody were added at an initial concentration of 500 nM. The plate was incubated at 37 °C overnight followed by washing 3 times to remove unconjugated proteins. About 100 μL of horseradish peroxidase (HRP)-conjugated anti-His antibody (ab1187, Abcam) and the chromogenic substrate were successively added for incubation. At the predetermined time points, reactions were stopped and an optical density of 450 nm was measured by a microplate reader.

Cells and animal models

All cell lines used in the experiment were obtained from the American Type Culture Collection (ATCC, USA). Normal intestinal epithelial cell line FHC was cultured in DMEM:F12 medium and human colorectal adenocarcinoma cell lines (HT-29, LS174-T) were cultured in RPMI-1640 medium. The medium was supplemented with 10% fetal bovine serum, 100 IU/mL penicillin and 100 μg/mL streptomycin.

The animal experiments were reviewed and approved by the animal welfare and ethics committees of the Fifth Affiliated Hospital of Sun Yat-sen University. All mice were purchased from the Animal Experiment Center of Guangdong Province (Guangzhou, China). To create a subcutaneous tumor, 5×10^6 cells suspended in 50 μL phosphate buffered saline (PBS) were mixed with 50% Matrigel (Corning, USA) and subcutaneously injected into the lateral thigh of BALB/c nude mice. Orthotopic model was established by orthotopic injection of 2×10^6 LS174-T-luc cells in 25 μL mixture of PBS and Matrigel into the colon wall of the mice. To simulate LNM in CRC, 2×10^6 LS174-T-luc cells were injected into the hock region of the mice. Inflammatory lymph node formation was induced by intramuscular injection of 10 μL of turpentine into the thighs of the mice. The successful construction of the orthotopic and LNM model were monitored using an *in vivo* imaging system (IVIS) apparatus (PerkinElmer, USA) after intraperitoneal injection of D-luciferin (PerkinElmer, USA) at a concentration of 150 mg/kg per body weight.

Western blot

Cells were lysed and the protein supernatant was collected by centrifuging at 12,000 g for 0.5 h. The concentration was quantified by a BCA Protein Quantitation Kit (Thermo Fisher Scientific, USA). About 30 μg of protein was loaded for SDS-PAGE, followed by transferring onto a polyvinylidene fluoride membrane. The membrane was blocked with 5% skim milk and then incubated with primary anti-CEACAM5 antibody (ab91213, Abcam) and anti-GAPDH antibody (#2118, CST) at 4 °C overnight. Then, the membrane was incubated with an HRP-conjugated secondary antibody (#7074, CST) and the protein band was eventually visualized with an enhanced chemiluminescence system.

Immunofluorescence staining

For immunocytochemistry, approximately 1×10^5 cells were seeded on a coverslip. After blocking with 1% bovine serum albumin (BSA), the cells were incubated with 1–2 μg/mL of nanobody and anti-CEACAM5 antibody (ab91213, Abcam) for 1 h at room temperature (RT). The slices were then visualized using Alexa Fluor 647-conjugated antibody (ab150115, Abcam) coupled with Dylight 488-conjugated anti-His tag antibody (1:1000, ab117512, Abcam) at RT for 0.5 h. Subsequently, the cells were incubated with DAPI and fluorescence was captured by confocal microscope (Zeiss880, Carl Zeiss, Germany).

For tissue immunofluorescence, dissected tumors were fixed with paraformaldehyde and embedded with O.C.T. Compound (Sakura Finetek, USA). The tissue was frozen in liquid nitrogen and cut into 5-mm sections. Subsequent procedures were similar to immunocytochemistry.

Flow cytometry

The cells were harvested with Accutase (Sigma, USA) and suspended with cold PBS. After being blocked by 3% BSA, the cells were incubated with nanobody or anti-CEACAM5 antibody for 1 h at RT. After washing 5 times with cold PBS, the cells were then incubated with FITC-labeled anti-His tag secondary antibody (ab1206, Abcam) in the dark for 30 min at RT. Thereafter, the cells were washed again and the fluorescence intensity was analyzed using a Beckman CytoFLEX flow cytometer (Beckman, USA) and FlowJo software (BD, USA).

Immunohistochemistry

Approval for the use of human samples was obtained from the Ethics Review Committee of the Fifth Affiliated Hospital of Sun Yat-sen University with waiver of informed consents (K170-1). Paraffin blocks were cut into 3-μm sections and deparaffinized in dimethylbenzene and dehydrated by serial immersion in gradient concentrations of alcohol. Antigen retrieval was performed under high pressure for 10 min. After blocking, the slices were incubated with anti-CEACAM5 antibody (1:200, ab91213, Abcam) overnight at 4 °C. The next day, the samples were incubated with an

HRP-conjugated secondary antibody (MaxVision, China) at RT for 30 min. Chromogenic reaction was performed using the DAB Kit (MaxVision, China) and counterstained with hematoxylin. The IHC images were captured by a slide Scanner System (3DHISTECH, Hungary) and H-score was quantified by 3DHISTECH QuantCenter software (3DHISTECH, Hungary).

Radiolabeling

Detailed radiolabeling method was elaborated in the previous literature [16, 17]. Briefly, ethyl-(4-trimethylammonium) benzoate trifluoromethanesulfonate was synthesized for subsequent synthesis of N-succinimidyl 4-[^{18}F] fluorobenzoate (^{18}F-SFB). For the conjugation reaction, nanobody (200—500 µg) in 300 µL of borate buffer (0.1 M, pH 7.4—9.0) was added into the reaction vial with dried ^{18}F-SFB (1.0—7.5 GBq). After incubation for 25 min at RT, the reaction mixture was purified using a PD-10 column (GE, USA) for further assessment by thin-layer chromatography (TLC). For the animal studies, the products were blown to dryness by nitrogen stream and redissolved with saline.

PET/CT imaging

MicroPET imaging was performed on a microPET scanner (Siemens, Germany). After tail vein injection of approximately 7.4 MBq (200 µCi) of ^{18}F-FB-Nb41 or ^{18}F-FB-Nb41-ABD, tumor-bearing mice were anesthetized and scanned under administration of 2% isoflurane (Sigma, USA) and static images at 0.5, 1, 2 and 4 h post-injection were acquired. For LNM models, mice were anesthetized and scanned 2 h post-injection. The images were processed using Carimas software. Regions of interest (ROI) were drawn and the uptake value was obtained. The radioactive uptake was quantified as percent injected dose per gram (%ID/g) assuming tissue density as 1 g/cm^3. The subcutaneous tumor-bearing mice were sacrificed after imaging. Tumor and main organs were weighed and the radioactivity was measured by a γ-counter (PerkinElmer, USA) to calculate their mean organ distribution. The uptake in the tissues was decay-corrected and expressed as %ID/g.

NIR fluorescence imaging

Nanobodies (in 500 µL PBS) were mixed with 1 mg/mL IRDye800CW NHS Ester (LI-COR, USA) at a molar ratio of 1:2 in the dark for 2 h. The excess dye was removed using a PD-10 column (GE, USA). The concentrations of the synthesized probe and synthesis efficiencies were measured using a NanoDrop 2000 UV–Vis spectrophotometer (Thermo Fisher Scientific, USA) at absorbance of 280 and 780 nm.

The tumor-bearing mice were intravenously injected with 50 µg of the synthesized probe. The images at different time points were captured using an IVIS Lumina III imaging system (PerkinElmer, USA) with an excitation and emission wavelength of 760 nm and 845 nm. The IVIS image processing software was used to measure the mean fluorescence intensity (MFI). After imaging, the mice were executed and the tumor as well as the main organs were harvested for *ex vivo* fluorescence imaging with the same parameters.

Statistical analysis

Statistical analyses were performed using Prism 7.0 (Graphpad, USA) and SPSS 19.0 (IBM, USA). Continuous variables were presented as mean ± standard deviation (Sd). The difference between groups were tested for significance using the two-sided Student's t test or one-way analysis of variance (ANOVA). P-values less than 0.05 were considered to be statistically significant (*$P < 0.05$, **$P < 0.01$, ***$P < 0.001$).

Results

IHC analysis in human CRC samples and metastatic lymph nodes (mLNs)

CEACAM5 expression profile based on TCGA/GTEx datasets indicated that *CEACAM5* expression in CRC was the highest among all types of cancer (Figure S1A), while *CEACAM5* expression was significantly higher in either colon adenocarcinoma or rectum adenocarcinoma than in normal tissues at the transcriptional level (Figure S1B). Clinical Proteomic Tumor Analysis Consortium (CPTAC) and the International Cancer Proteogenome Consortium (ICPC) datasets also showed that CEACAM5 protein expression was significantly higher in CRC than normal tissues (Figure S1C). IHC was applied to verify the expression of CEACAM5 from human CRC patients (n = 115). Among them, 41 patients showed LNM. Representative images of human primary CRC and corresponding mLNs stained with anti-CEACAM5 antibody showed that CEACAM5 was overexpressed in CRC specimens and their corresponding mLNs (Fig. 1A, B), with positive rates of 95.7% (110/115) and 97.6% (40/41). Quantitative analysis showed that CEACAM5 expression in tumor tissues was significantly higher than adjacent tissues (H-score, 171.7 ± 53.35 vs. 26.54 ± 15.22, $P < 0.0001$, Fig. 1C). Linear correlation analysis showed that CEACAM5 expression in mLNs was significantly associated with CEACAM5 expression in the primary tumor, with a Pearson correlation coefficient of 0.68 ($P < 0.0001$, Fig. 1D). As illustrated in Table S1, CEACAM5 expression was not correlated with clinicopathologic

Fig. 1 CEACAM5 expression in human CRC samples and mLNs. **A**, **B** Representative CEACAM5 staining images of tumor tissues and mLNs from CRC patients (-: negative, +: weak positive, + +: medium positive, + + +: strong positive. Scale bars: above, 2000 μm; below, 20 μm). **C** Quantitative analysis of the immunohistochemical results of tumor tissues and mLNs. **D** Correlation analysis of respective H-score of tumor tissues and mLNs (*r*, correlation coefficient)
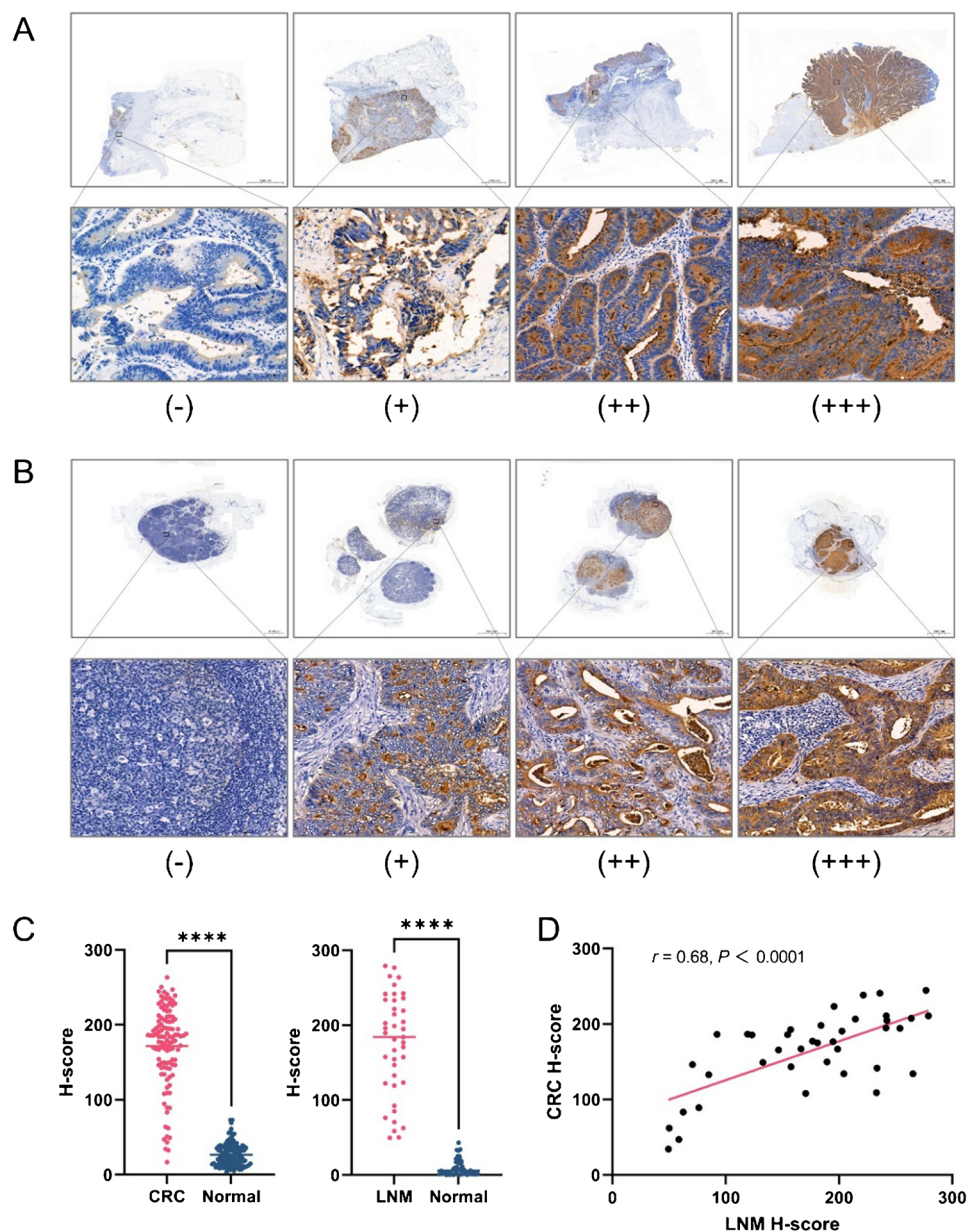
parameters, such as age, gender, tumor location, lymph nodes metastasis, AJCC stage and different differentiation ($P > 0.05$). These results suggested that CEACAM5 may serve as an appealing marker for imaging of CRC.

Expression and purification of CEACAM5 targeted nanobodies

Figure 2A illustrated the schematic overview of nanobody screening, identification and expression. Significantly higher antibody level in the serum of the dromedary was observed after antigen immunization (Fig. 2B). After several rounds of screening, the positive clones with relatively high OD values were selected to be sequenced, and we finally picked the clone with duplicated sequence No.41 as the final target, abbreviated as Nb41 (Figure S2A). The resulting nanobodies after each purification step were visualized on a Coomassie blue-stained gel, indicating that the nanobody was mainly expressed in periplasm (Fig. 2C). A unique band with an approximate molecular weight of 16 kDa, as expected for the size of a nanobody, can be seen after purifying (Fig. 2C). The SEC curve revealed a unique symmetric peak (Figure S2B), reflecting high purity of the nanobody. Figure 2D showed the sequence diagram of the complementarity determining regions (CDRs) and corresponding structure of Nb41. Derived from dromedary antibodies, nanobodies are only one-tenth of the size of an intact antibody (Fig. 2E).
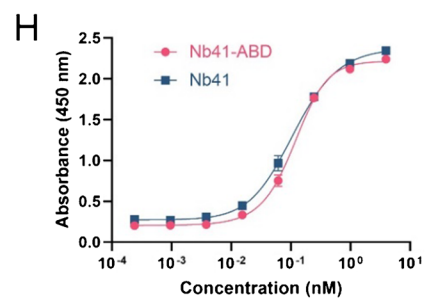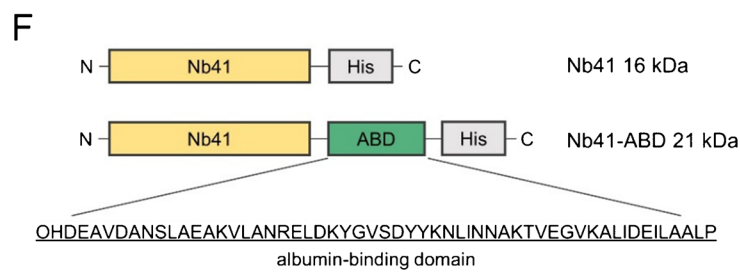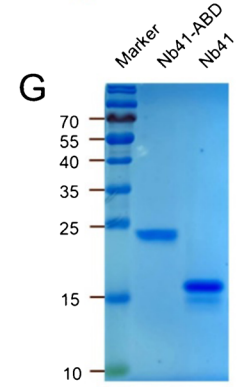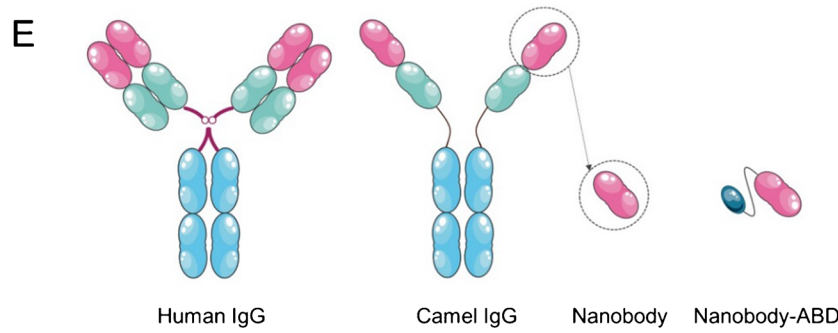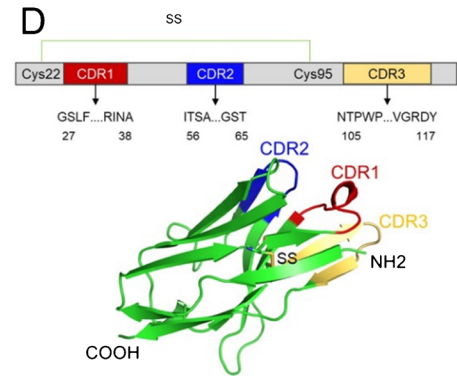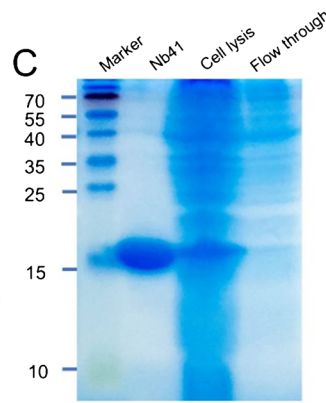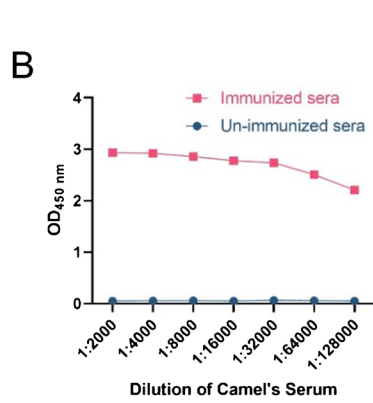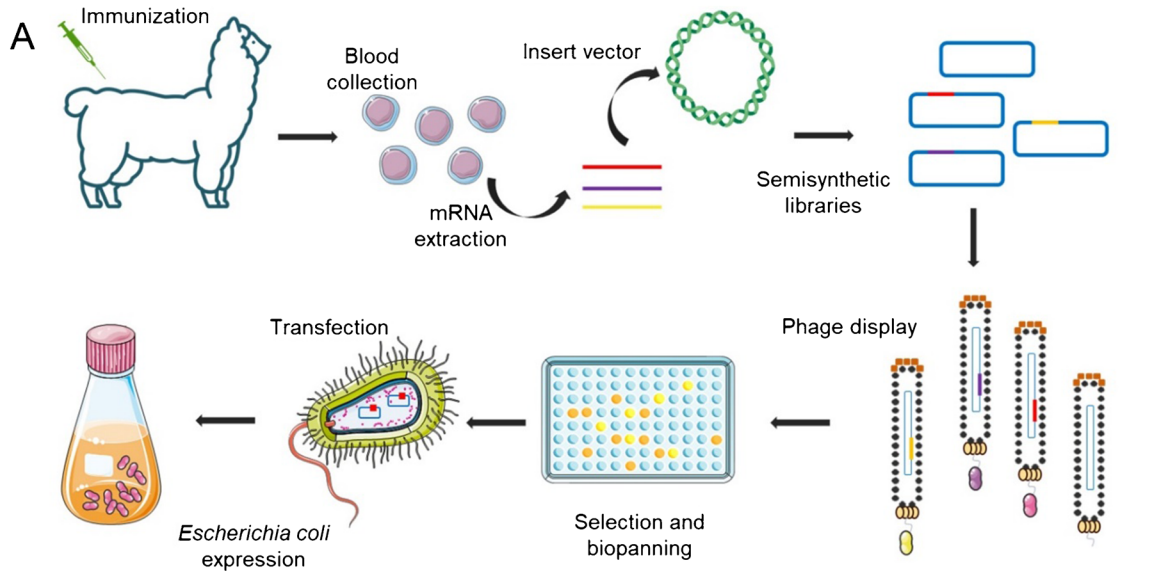
◄**Fig. 2** Identification, expression and purification of CEACAM5 targeted nanobodies. **A** Schematic overview of nanobody generation. **B** Serum antibody changes in the dromedary with or without antigen immunization. **C** Coomassie blue staining of *E. coli* lysate, flowthrough solution and nanobodies after purification. Unit: kDa. **D** A sequence diagram of the complementarity determining region (CDR) and corresponding structure of Nb41. **E** Comparison of nanobody and an intact antibody. **F** Sequence diagrams of Nb41 and Nb41-ABD. **G** Coomassie blue staining of Nb41 and Nb41-ABD. Unit: kDa. **H** Comparison of the binding affinity of Nb41 and Nb41-ABD by ELISA

As shown in Fig. 2F, a naturally derived ABD found in protein G was added into the C-terminal amino acid of Nb41 to create Nb41-ABD [18], with an approximate molecular weight of 22 kDa (Fig. 2G). The dissociation constant (Kd) of Nb41-ABD determined by ELISA varied little from Nb41 (0.21 nM vs. 0.14 nM, Fig. 2H). The cytotoxicity of the generated nanobodies were tested by cell counting kit-8 (CCK8) assay. As exhibited in Figure S2C, no obvious cytotoxicity was observed in LS174-T cells with the increase of concentrations of the nanobody after incubation for 48 h.

Binding of CEACAM5 targeted nanobodies to CRC cells *in vitro*

As demonstrated by Western blot, high expression of CEACAM5 was observed in LS174-T, while it was almost not expressed in HCT-116 and normal colorectal epithelial FHC cells (Fig. 3A). Flow cytometry and confocal microscopy were conducted to determine the target-specificity of nanobodies to CRC cells. Confocal imaging showed that Nb41 colocalized with CEACAM5 in the cytomembrane of LS174-T rather than FHC and HCT-116 cells (Fig. 3B). Consistent with immunofluorescence, flow cytometry analysis showed significant peak shift in both Nb41 and Nb41-ABD treated LS174-T cells, compared to FHC and HCT-116 cells (Fig. 3C). Quantitative analysis showed that Nb41 and Nb41-ABD were on par with each other in terms of their ability to bind to cells (Fig. 3D). These findings elucidated that CEACAM5 is the primary target of Nb41 and Nb41-ABD, suggesting that the CEACAM5 targeted nanobodies may serve as ideal targeted molecules for molecular imaging of CRC.

PET imaging of CRC subcutaneous xenografts

Detailed synthesis routes of the labeling precursor ^{18}F-SFB were elaborated in Figure S3A. After labeling, the TLC scanning results showed that the peak of ^{18}F-SFB was significantly reduced compared with that before labeling, indicating that the complex was successfully generated, with a radiochemical purity more than 98% (Figure S3B). The labeling yields of ^{18}F-FB-Nb41-ABD and ^{18}F-FB-Nb41 were

calculated to be $64.2 \pm 4.7\%$ and $69.2 \pm 2.0\%$ (not attenuation corrected). The specific activities of ^{18}F-FB-Nb41-ABD and ^{18}F-FB-Nb41 were calculated to be 15.14 ± 0.34 and 14.64 ± 0.44 GBq/μmol, respectively. The binding specificity was confirmed by blocking assay, suggesting that the binding of ^{18}F-FB-Nb41 and ^{18}F-FB-Nb41-ABD to the cells was mediated by the nanobodies (Figure S3C). The *in vitro* stability of ^{18}F-FB-Nb41 in serum and saline was demonstrated with a radiochemical purity still greater than 96% after incubation for 2 h (Figure S3D, E).

In LS174-T-bearing subcutaneous mice, both ^{18}F-FB-Nb41 and ^{18}F-FB-Nb41-ABD showed gradual accumulation in the tumor and relatively low uptake in peripheral organs and tissues over time, with tumor uptakes quantified as 3.97 ± 0.25 and $6.53 \pm 0.99\%$ID/g at 4 h post-injection (Fig. 4A). Due to the longer retention time in the blood pool, ^{18}F-FB-Nb41-ABD enrichment in tumors was significantly delayed compared with ^{18}F-FB-Nb41 (Fig. 4B). In addition to the kidneys, ^{18}F-FB-Nb41 appears to be more prevalent in the liver, spleen and lungs while ^{18}F-FB-Nb41-ABD was more likely to be prevalent in the liver, spleen and heart (Figure S4A, B). These results were corroborated by biodistribution analysis (Fig. 4C, Table S2, Table S3). Tumors were harvested for IHC and immunofluorescence staining 24 h after imaging until the radioactivity decayed to a negligible dose. CEACAM5 was observed to be highly expressed in tumor according to IHC staining (Fig. 4D). Confocal imaging revealed that the nanobodies colocalized with CEACAM5 in the cytomembrane of the tumor cells, suggesting the enrichment of nanobodies in the tumor (Fig. 4E). Similarly, the radioactively labeled nanobody ^{18}F-FB-Nb41 showed an enrichment in the orthotopic tumor (Figure S4C). The successful construction of the orthotopic tumor was determined by bioluminescence imaging and gross anatomy (Figure S4C). These results indicated that CEACAM5-targeted nanobodies exhibited superior imaging effects and could be used for PET imaging in CRC.

PET imaging of LNM with ^{18}F labeled nanobody

Considering the high expression of CEACAM5 in mLNs of CRC, we further validated the imaging efficacy of CEACAM5-targeted nanobody probes in LNM models. As representative PET images shown in Fig. 5A, both ^{18}F-FB-Nb41 and ^{18}F-FB-Nb41-ABD showed prominent mLNs enrichment in LNM models. In contrast to ^{18}F-FB-Nb41, ^{18}F-FB-Nb41-ABD showed relatively higher mLNs enrichment (5.13 ± 0.51 vs. $3.97 \pm 0.30\%$ID/g, Fig. 5B). As depicted by gross anatomy and magnetic resonance imaging (MRI), the LNM models were successfully constructed (Fig. 5C). To further substantiate the existence of the LNM, mice were sacrificed and the lymph nodes were harvested 24 h after imaging. H&E staining confirmed the successful
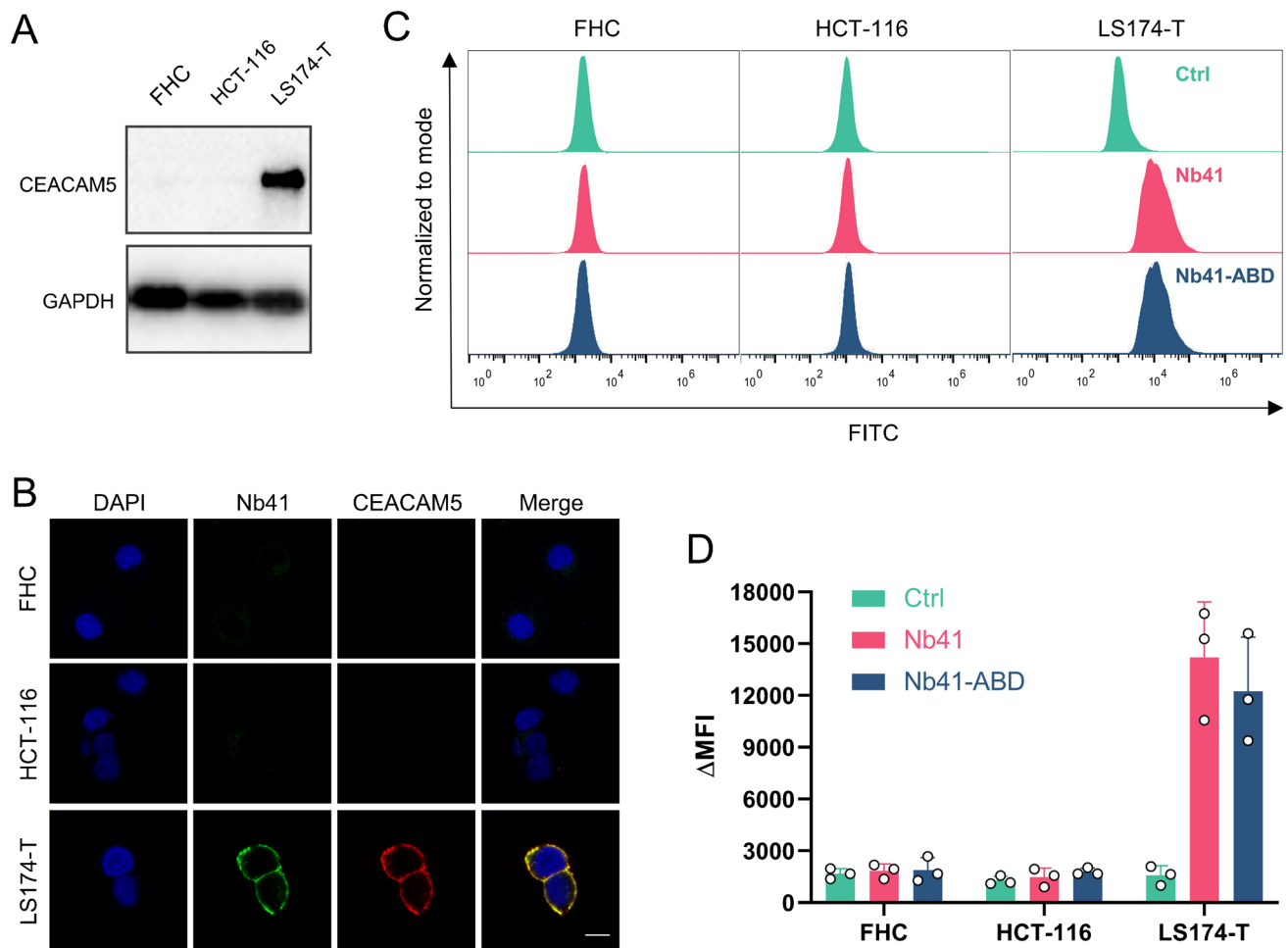
Fig. 3 Binding of CEACAM5 targeted nanobodies to colorectal cells. **A** CEACAM5 expression in different cell lines. **B** Confocal fluorescence imaging of the cellular binding of Nb41 to different cell lines. Scale bar, 10 µm. **C, D** Flow cytometry and quantitative analysis of the cell binding of Nb41 and Nb41-ABD. ΔMFI, relative mean fluorescence intensity

construction of LNM, while IHC staining revealed high expression of CEACAM5 in LNM (Fig. 5D). Intriguingly, ^{18}F-FB-Nb41 and ^{18}F-FB-Nb41-ABD did not show an iota of enrichment in inflammatory lymph nodes, where ^{18}F-FDG showed significant enrichment (Figure S4D). The successful induction of inflammatory lymph nodes was verified by gross anatomy and MRI. This suggested that the ^{18}F-labeled nanobody provided a unique advantage in identifying tumor LNM and inflammatory lymph nodes with ^{18}F-FDG, a widely used radioactive agent in clinical practice.

NIR imaging of CRC subcutaneous xenografts

Nanobodies were coupled to IRDye800CW (IR800) to form NIR conjugates (Nb41-IR800 or Nb41-ABD-IR800) (Figure S5A). The peaks at 280 nm and 780 nm of absorption spectrum represented the nanobody and IR800, respectively, indicating the successful synthesis of the NIR probe (Figure S5B). As the NIR images in LS174-T xenograft tumor models

summarized in Fig. 6A, Nb41-IR800 and Nb41-ABD-IR800 accumulated in the tumor over time. Compared to Nb41-IR800, Nb41-ABD-IR800 exhibited higher fluorescence intensity in the tumor, with a remarkably delayed time to reach the peak (4 h vs 2 h post-injection). Despite the fact that the overall fluorescence intensity of the two probes *in vivo* decreased over time, Nb41-ABD-IR800, as it slowly cleared from the blood, maintained excellent tumor-to-background ratios (TBR) compared to Nb41-IR800 (Fig. 6B, C). Significant fluorescence signal reduction at tumor sites after simultaneous injection of tenfold dye-free labeled nanobodies was observed in both Nb41-IR800 or Nb41-ABD-IR800 group, indicating superior tumor targeting specificity of the two probes (Fig. 6D). These were also validated by *ex vivo* fluorescence imaging of the main organs and the tumors (Figure S5C-F). *Ex vivo* fluorescence imaging of the main organs and the tumors was performed to further investigate the biodistribution of the probes. A stronger fluorescent signal can be seen in tumors with either injection of Nb41-IR800 or Nb41-ABD-IR800 (Fig. 6E, F).

Fig. 4 PET imaging of CRC subcutaneous xenografts using ^{18}F labeled nanobody. **A** Representative PET images of the multi-time-points PET imaging post-injection of ^{18}F-FB-Nb41 or ^{18}F-FB-Nb41-ABD, respectively (n = 3). **B** Radiation uptakes of the tumors over time. **C** The radioactive biodistribution of ^{18}F-FB-Nb41 or ^{18}F-FB-Nb41-ABD in the tumors and major organs (n = 3). **D** Representative CEACAM5 staining images of tumor tissues resected from LS174-T tumor-bearing mice. Scale bar: left, 2000 μm; right, 20 μm. **E** Confocal fluorescence imaging of the tumor tissues resected from LS174-T tumor-bearing mice. Scale bar, 10 μm
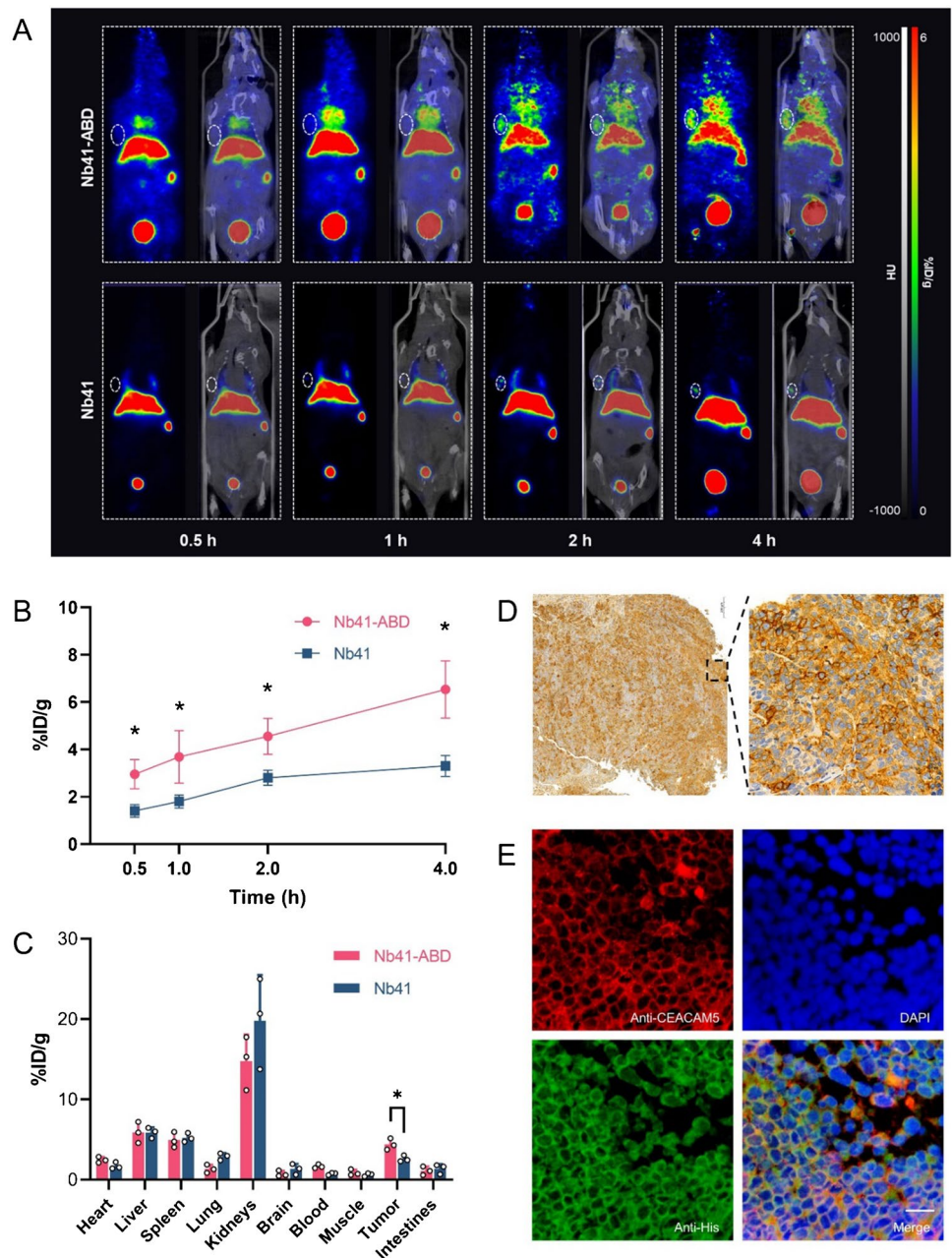
Compared with Nb41-IR800, which is mainly metabolized by the kidney, Nb41-ABD-IR800 also showed a high fluorescence signal in the liver at 4 h after injection (Fig. 6E, F). All these results implied that CEACAM5-targeted nanobodies exhibited superior imaging effects and could be used for NIR imaging in CRC subcutaneous models.

Discussion

Here in our study, as a preclinical proof-of-concept, we identified a CEACAM5 targeted nanobody, with excellent *in vitro* binding properties. Incorporation of ABD did not affect the affinity of Nb41. The CEACAM5-targeted nanobodies exhibited prominent tumor and LNM enrichment in CRC subcutaneous xenografts models and LNM models. Similarly, the IR800-conjugated nanobodies exhibited superior imaging effects in subcutaneous models. To sum up, we presented the identification and *in vivo* validation of a CEACAM5-targeted nanobody and a fused nanobody with an ABD, which enabled the non-invasive visualization of malignancy of CRC using PET imaging and NIR imaging. This will later facilitate the full management of CRC patients. Namely, CEACAM5-targeted PET imaging can noninvasively characterize the extent of the disease to determine whether the patient is a candidate for surgery,

Fig. 5 PET imaging of LNM with ^{18}F labeled nanobody probes. **A** Representative PET images in LNM models post-injection of ^{18}F-FB-Nb41 or ^{18}F-FB-Nb41-ABD (n = 3). **B** Quantification of the LNM in PET imaging. **C** Gross anatomy and MRI of LNM after PET imaging. **D** Representative IHC and H&E staining images of LNM resected from mice. Scale bar: above, 40 μm; below, 20 μm
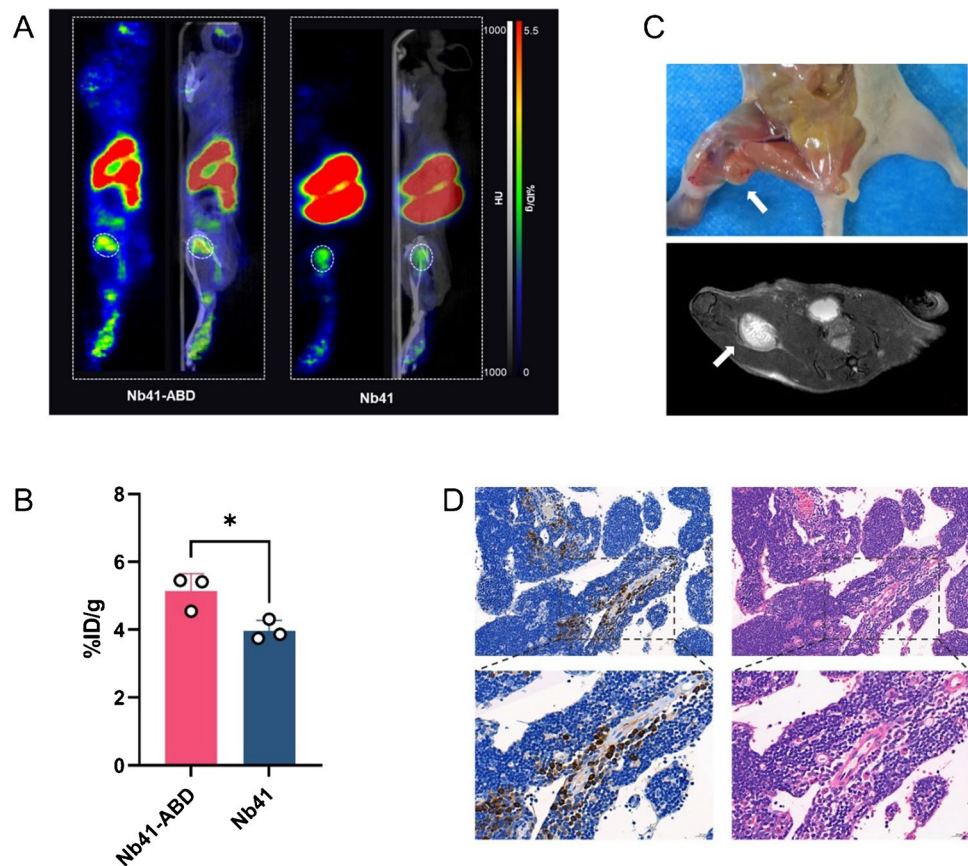
while intraoperative NIR imaging could visualize otherwise invisible tumor margins.

Intact antibodies, with an *in vivo* circulation time more than several weeks, often display superior imaging due to prominent tumor enrichment [9, 10]. Nevertheless, this property of full-length immunoglobulins typically militates against radiographic imaging as it may result in non-targeted radioactive damage when labeled with long half-life nuclides. Due to the slow kinetics of mAbs in humans, a larger time window should be considered for imaging after 24 to 96 h after intravenous injection of the contrast agent [19]. Nanobodies, while preserving comparable affinity to intact antibodies, are smaller in size, allowing for enhanced tumor penetration and shorter circulation times. In fact, the application is somewhat circumscribed by their rapid renal clearance. Therefore, we optimized the half-life of the nanobody through the introduction of ABD, which contributes to higher tumor enrichment. Adapted to the faster clearance time of the nanobodies *in vivo*, ^{18}F was opted as the labeled radionuclide due to its favorable physical advantages (109.8 min half-life) [20]. In our study, non-covalent interaction with albumin through the incorporation of an ABD significantly increased the extent of the half-life of the nanobodies in the blood pool, which contributed to higher tumor uptakes. With the radioactivity in the blood pool gradually

decreasing and the tumor uptake gradually increasing over time, an ideal tumor background ratio of the ABD fused probe can be obtained at subsequent times (> 4 h). Unfortunately, due to the short half-life of ^{18}F, we were unable to obtain PET images with longer time. Replacing it with a longer half-life nuclide, such as ^{64}Cu for imaging is one of the next studies we are conducting.

As a preclinical study, our project focused on the development of CEACAM5-targeting nanobodies and preliminary application of nanobody-based molecular probes at the animal level, which is an essential step for clinical translation. Application of our molecular probes in clinical trials is one of our next major research directions. As for the concerns about tumor uptake, ^{18}F-FB-Nb41

Fig. 6 NIR imaging in mice bearing subcutaneous LS174-T tumor. **A** Representative NIR images post-injection of Nb41-ABD-IR800 or Nb41-IR800 (n = 4). **B, C** The mean fluorescence intensity (MFI) and tumor-to-background ratios (TBR) of the tumors. The mini-graph above the main graph is a magnification of the preceding time points. **D** Representative NIR images and the MFI quantification of the NIR-probe group and block group. Mice in block group were simultaneously injected with tenfold dye-free labeled Nb41 or Nb41-ABD. **E, F** NIR images and the MFI quantification of the resected tumors and major organs 4 h or 2 h post-injection (n = 4). From left to right and from top to bottom, the major organs were brain, bone, heart, colon, blood, kidneys, spleen, muscle, pancreas, skin, liver, lungs, stomach and tumor, respectively
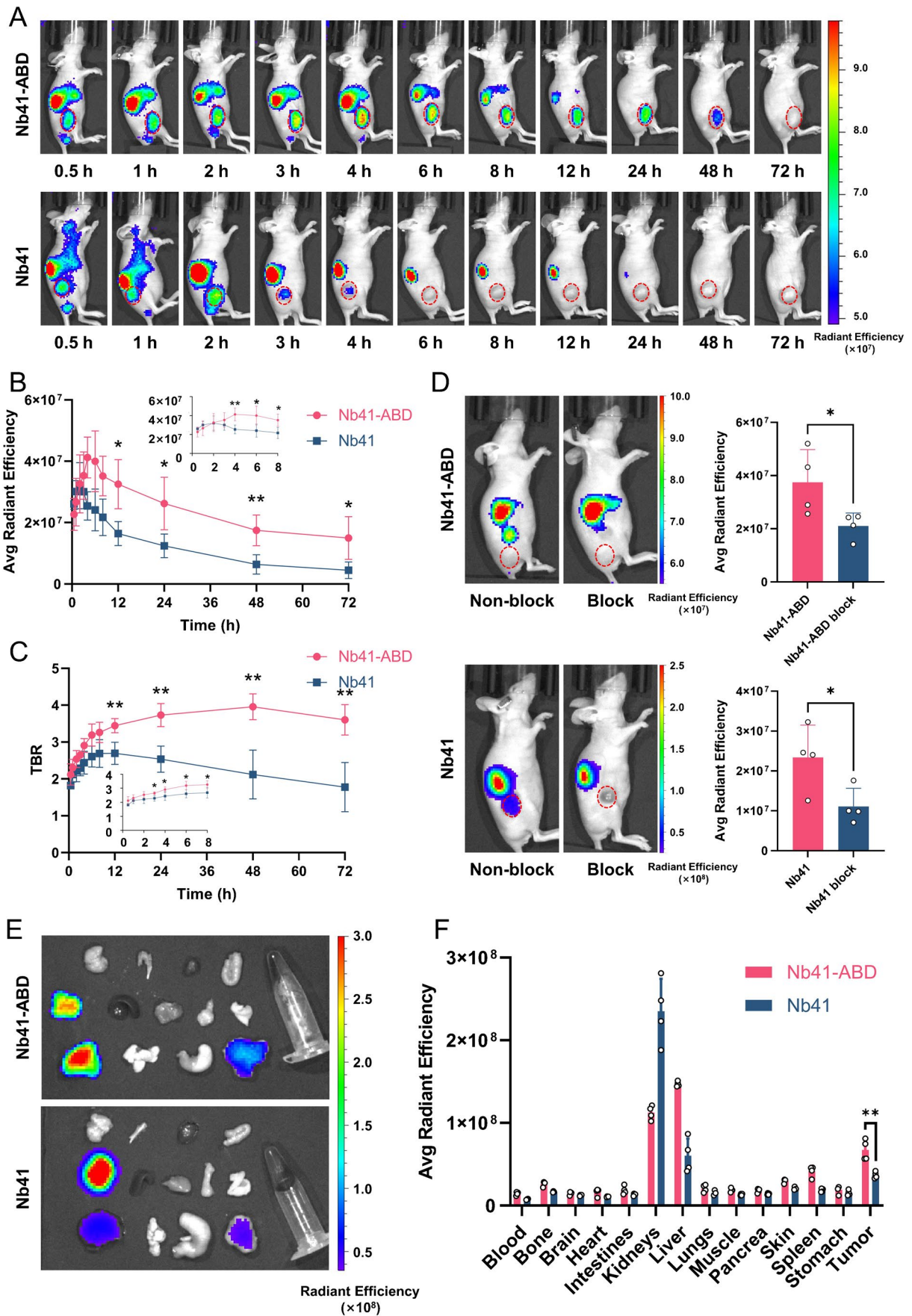
and ^{18}F-FB-Nb41-ABD in the tumors were quantified as 3.97 ± 0.25 and 6.53 ± 0.99%ID/g at 4 h post-injection, which is similar to other nanobody-based radiotracer that have entered human trials [21]. It is worth noting that the uptake of the radiotracers in liver is slightly higher than in tumor. This may be inconsequential for tumor imaging, since several nanobody-based tracers all demonstrated correspondingly high liver uptake [22–24]. A compelling interpretation could be that the reticuloendothelial system in the liver and spleen accumulated the associated sum of activities [25]. In addition to traditional methods, for instance, PEGylation and site-specific labeling, some new strategies such as pre-targeted system and clearance-enhanced system have also made headway to reduce unexpected liver uptake [26].

As the most common metastasis site of CRC, the mLNs appear in approximately 35% of CRC patients, which substantially decreases the likelihood of cure [27]. Current clinical guidelines consider the presence of LNM as one of the most potent prognostic indicators of CRC [28]. More than 70% patients with T1 CRC were considered to be at high risk, yet post-operative pathology shows that only 5%-15% of them ultimately occurred LNM [29]. Therefore, determination of LNM has become essential to select those with truly high-risk diseases, while avoiding overtreatment of other patients. Our study demonstrated that both ^{18}F-FB-Nb41 and ^{18}F-FB-Nb41-ABD showed prominent LNM enrichment in LNM models, which allowed for a further accurate depiction of tumor LNM in CRC patients. More importantly, due to antigen specificity, CEACAM5-targeted nanobody probes were able to discriminate between tumor LNM and inflammatory lymph nodes, which also typically exhibit non-specific uptake with ^{18}F-FDG, a widely used radioactive agent in clinical practice [30].

Previous efforts have sought to find high-performance NIR fluorescent targeted agents for fluorescence-guided surgery. So far, mAbs were considered to be the best option to form an NIR probe. Yet, preliminary data suggested that intraoperative imaging applying dye-conjugated mAbs should be carried out several days post-injection, which led to delays in treatment and waste of resources from a logistical standpoint [31]. In contrast, the nanobody-based probe could be administered into a patient a few hours prior to the surgery. As expected, our nanobody-based NIR tracers obtained prominent tumor enrichment within a few hours, with favorable tumor to background ratios being obtained over time. This allowed for more precise and specific identification of CRC, and assists surgeons in developing tailored tumor resections.

It is foreseeable that CEACAM5-targeted nanobodies will serve a wider range of applications in the forthcoming future. The IR800 conjugated nanobody probes, with their NIR in the second window (NIR-II), will potentially be available for NIR-II imaging of CRC, since NIR-II provides better tissue penetration and signal contrast [10]. In addition to CRC, CEACAM5-targeted probes may also potentially be applicable for other CEACAM5-overexpressing malignancies, since CEACAM5 was reported to be highly expressed in gastric, pancreatic, esophageal, lung, breast malignancies and their concomitant mLNs [32]. Another potential application pertains to nanobody based chimeric antigen receptor T-cell (CAR-T) therapy. As single-chain variable fragment usually leads to host immune system-mediated immunogenicity and self-aggregation induced CAR-T exhaustion [33], nanobody-based CAR-T therapy is expected to circumvent the limitations in the immunotherapy of CEACAM5-positive tumors.

Conclusion

Collectively, we developed a high-affinity CEACAM5 targeted nanobody and optimized its circulation by fusing an ABD, which enables to the non-invasive visualization of malignancy of CRC using PET and NIR imaging in subcutaneous tumors and mLNs. Moving forward, we sincerely hope that this new targeted probe may be valuable for staging guidance and surgical intervention in CRC patients.

Declarations

Affiliated Hospital of Sun Yat-sen University with waiver of informed consents (K170-1).

References

1. Bray F, Ferlay J, Soerjomataram I, Siegel RL, Torre LA, Jemal A. Global cancer statistics 2018: GLOBOCAN estimates of incidence and mortality worldwide for 36 cancers in 185 countries. CA Cancer J Clin. 2018;68(6):394–424. https://doi.org/10.3322/caac.21492.

2. Ulintz PJ, Greenson JK, Wu R, Fearon ER, Hardiman KM. Lymph Node Metastases in Colon Cancer Are Polyclonal. Clin Cancer Res. 2018;24(9):2214–24. https://doi.org/10.1158/1078-0432.CCR-17-1425.

3. Rigo P, Paulus P, Kaschten BJ, Hustinx R, Bury T, Jerusalem G, et al. Oncological applications of positron emission tomography with fluorine-18 fluorodeoxyglucose. Eur J Nucl Med. 1996;23(12):1641–74. https://doi.org/10.1007/BF01249629.

4. Kostakoglu L, Hardoff R, Mirtcheva R, Goldsmith SJ. PET-CT fusion imaging in differentiating physiologic from pathologic FDG uptake. Radiographics. 2004;24(5):1411–31. https://doi.org/10.1148/rg.245035725.

5. Te VE, Veerman T, Subramaniam V, Ruers T. The use of fluorescent dyes and probes in surgical oncology. Eur J Surg Oncol. 2010;36(1):6–15. https://doi.org/10.1016/j.ejso.2009.10.014.

6. Barnett T, Goebel SJ, Nothdurft MA, Elting JJ. Carcinoembryonic antigen family: characterization of cDNAs coding for NCA and CEA and suggestion of nonrandom sequence variation in their conserved loop-domains. Genomics. 1988;3(1):59–66. https://doi.org/10.1016/0888-7543(88)90160-7.

7. Gold P, Freedman SO. Specific carcinoembryonic antigens of the human digestive system. J Exp Med. 1965;122(3):467–81. https://doi.org/10.1084/jem.122.3.467.

8. Colcher D, Esteban J, Mornex F. Use of monoclonal antibodies as radiopharmaceuticals for the localization of human carcinoma xenografts in athymic mice. Methods Enzymol. 1986;121:802–16. https://doi.org/10.1016/0076-6879(86)21078-2.

9. Liang M, Yang M, Wang F, Wang X, He B, Mei C, et al. Near-infrared fluorescence-guided resection of micrometastases derived from esophageal squamous cell carcinoma using a c-Met-targeted probe in a preclinical xenograft model. J Control Release. 2021;332:171–83. https://doi.org/10.1016/j.jconrel.2021.02.019.

10. Wang L, Liang M, Xiao Y, Chen J, Mei C, Lin Y, et al. NIR-II Navigation with an EGFR-Targeted Probe Improves Imaging Resolution and Sensitivity of Detecting Micrometastases in Esophageal Squamous Cell Carcinoma Xenograft Models. Mol Pharm. 2022;19(10):3563–75. https://doi.org/10.1021/acs.molpharmaceut.2c00115.

11. Xiao YT, Zhou C, Ye JC, Yang XC, Li ZJ, Zheng XB, et al. Integrin alpha6-Targeted Positron Emission Tomography Imaging of Colorectal Cancer. ACS Omega. 2019;4(13):15560–6. https://doi.org/10.1021/acsomega.9b01920.

12. Mcmahon C, Baier AS, Pascolutti R, Wegrecki M, Zheng S, Ong JX, et al. Yeast surface display platform for rapid discovery of conformationally selective nanobodies. Nat Struct Mol Biol. 2018;25(3):289–96. https://doi.org/10.1038/s41594-018-0028-6.

13. Wolfson W. Ablynx makes nanobodies from llama bodies. Chem Biol. 2006;13(12):1243–4. https://doi.org/10.1016/j.chembiol.2006.12.003.

14. Dennis MS, Jin H, Dugger D, Yang R, Mcfarland L, Ogasawara A, et al. Imaging tumors with an albumin-binding Fab, a novel tumor-targeting agent. Cancer Res. 2007;67(1):254–61. https://doi.org/10.1158/0008-5472.CAN-06-2531.

15. Vincke C, Gutiérrez C, Wernery U, Devoogdt N, Hassanzadeh-Ghassabeh G, Muyldermans S. Generation of Single Domain Antibody Fragments Derived from Camelids and Generation of Manifold Constructs. In: Chames P, editor. Antibody Engineering: Methods and Protocols. 2nd ed. Totowa, NJ: Humana Press; 2012. p. 145–76.

16. Hatanaka K, Asai T, Koide H, Kenjo E, Tsuzuku T, Harada N, et al. Development of double-stranded siRNA labeling method using positron emitter and its in vivo trafficking analyzed by positron emission tomography. Bioconjug Chem. 2010;21(4):756–63. https://doi.org/10.1021/bc9005267.

17. Vaidyanathan G, Zalutsky MR. Synthesis of N-succinimidyl 4-[18F]fluorobenzoate, an agent for labeling proteins and peptides with 18F. Nat Protoc. 2006;1(4):1655–61. https://doi.org/10.1038/nprot.2006.264.

18. Wei J, Bera TK, Liu XF, Zhou Q, Onda M, Ho M, et al. Recombinant immunotoxins with albumin-binding domains have long half-lives and high antitumor activity. Proc Natl Acad Sci U S A. 2018;115(15):E3501–8. https://doi.org/10.1073/pnas.1721780115.

19. de Gooyer JM, Elekonawo F, Bos DL, van der Post RS, Pelegrin A, Framery B, et al. Multimodal CEA-Targeted Image-Guided Colorectal Cancer Surgery using (111)In-Labeled SGM-101. Clin Cancer Res. 2020;26(22):5934–42. https://doi.org/10.1158/1078-0432.CCR-20-2255.

20. Wang Y, Lin Q, Shi H, Cheng D. Fluorine-18: Radiochemistry and Target-Specific PET Molecular Probes Design. Front Chem. 2022;10:884517. https://doi.org/10.3389/fchem.2022.884517.

21. Qin X, Guo X, Liu T, Li L, Zhou N, Ma X, et al. High in-vivo stability in preclinical and first-in-human experiments with [(18)F]AlF-RESCA-MIRC213: a (18)F-labeled nanobody as PET radiotracer for diagnosis of HER2-positive cancers. Eur J Nucl Med Mol Imaging. 2023;50(2):302–13. https://doi.org/10.1007/s00259-022-05967-7.

22. Wang C, Chen Y, Hou YN, Liu Q, Zhang D, Zhao H, et al. ImmunoPET imaging of multiple myeloma with [(68)Ga]Ga-NOTA-Nb1053. Eur J Nucl Med Mol Imaging. 2021;48(9):2749–60. https://doi.org/10.1007/s00259-021-05218-1.

23. Warnders FJ, Terwisscha VSA, Knuehl C, van Roy M, de Vries E, Kosterink J, et al. Human Epidermal Growth Factor Receptor 3-Specific Tumor Uptake and Biodistribution of (89)Zr-MSB0010853 Visualized by Real-Time and Noninvasive PET Imaging. J Nucl Med. 2017;58(8):1210–5. https://doi.org/10.2967/jnumed.116.181586.

24. Liu Q, Jiang L, Li K, Li H, Lv G, Lin J, et al. Immuno-PET imaging of (68)Ga-labeled nanobody Nb109 for dynamic monitoring the PD-L1 expression in cancers. Cancer Immunol Immunother. 2021;70(6):1721–33. https://doi.org/10.1007/s00262-020-02818-y.

25. D'Huyvetter M, Vincke C, Xavier C, Aerts A, Impens N, Baatout S, et al. Targeted radionuclide therapy with A 177Lu-labeled anti-HER2 nanobody. Theranostics. 2014;4(7):708–20. https://doi.org/10.7150/thno.8156.

26. Wei W, Rosenkrans ZT, Liu J, Huang G, Luo QY, Cai W. ImmunoPET: Concept, Design, and Applications. Chem Rev. 2020;120(8):3787–851. https://doi.org/10.1021/acs.chemrev.9b00738.

27. Wada Y, Shimada M, Murano T, Takamaru H, Morine Y, Ikemoto T, et al. A Liquid Biopsy Assay for Noninvasive Identification of Lymph Node Metastases in T1 Colorectal Cancer. Gastroenterology. 2021;161(1):151-162.e1. https://doi.org/10.1053/j.gastro.2021.03.062.

28. Jin M, Frankel WL. Lymph Node Metastasis in Colorectal Cancer. Surg Oncol Clin N Am. 2018;27(2):401–12. https://doi.org/10.1016/j.soc.2017.11.011.

29. Tamaru Y, Oka S, Tanaka S, Nagata S, Hiraga Y, Kuwai T, et al. Long-term outcomes after treatment for T1 colorectal carcinoma: a multicenter retrospective cohort study of Hiroshima GI Endoscopy Research Group. J Gastroenterol. 2017;52(11):1169–79. https://doi.org/10.1007/s00535-017-1318-1.

30. Heriot AG, Hicks RJ, Drummond EG, Keck J, Mackay J, Chen F, et al. Does positron emission tomography change management in primary rectal cancer? A prospective assessment Dis Colon Rectum. 2004;47(4):451–8. https://doi.org/10.1007/s10350-003-0089-3.

31. Kijanka M, Warnders FJ, El KM, Lub-De HM, van Dam GM, Ntziachristos V, et al. Rapid optical imaging of human breast tumour xenografts using anti-HER2 VHHs site-directly conjugated to IRDye 800CW for image-guided surgery. Eur J Nucl Med Mol Imaging. 2013;40(11):1718–29. https://doi.org/10.1007/s00259-013-2471-2.

32. Hammarstrom S. The carcinoembryonic antigen (CEA) family: structures, suggested functions and expression in normal and malignant tissues. Semin Cancer Biol. 1999;9(2):67–81. https://doi.org/10.1006/scbi.1998.0119.

33. Shah NN, Fry TJ. Mechanisms of resistance to CAR T cell therapy. Nat Rev Clin Oncol. 2019;16(6):372–85. https://doi.org/10.1038/s41571-019-0184-6.